Downloaded from orbit.dtu.dk on: Apr 16, 2024

DTU Library

Analysis of damage localization based on acoustic emission data from test of wind turbine blades

Mielke, Adam; Benzon, Hans-Henrik; McGugan, Malcolm; Chen, Xiao; Madsen, Henrik; Branner, Kim; Ritschel, Tobias K.S.

Published in:
Measurement: Journal of the International Measurement Confederation

Link to article, DOI:
10.1016/j.measurement.2024.114661

Publication date:
2024

Document Version
Publisher's PDF, also known as Version of record

Link back to DTU Orbit

Citation (APA):
Mielke, A., Benzon, H-H., McGugan, M., Chen, X., Madsen, H., Branner, K., & Ritschel, T. K. S. (2024). Analysis of damage localization based on acoustic emission data from test of wind turbine blades. *Measurement: Journal of the International Measurement Confederation*, *231*, Article 114661. https://doi.org/10.1016/j.measurement.2024.114661

General rights
Copyright and moral rights for the publications made accessible in the public portal are retained by the authors and/or other copyright owners and it is a condition of accessing publications that users recognise and abide by the legal requirements associated with these rights.

- Users may download and print one copy of any publication from the public portal for the purpose of private study or research.
- You may not further distribute the material or use it for any profit-making activity or commercial gain
- You may freely distribute the URL identifying the publication in the public portal

If you believe that this document breaches copyright please contact us providing details, and we will remove access to the work immediately and investigate your claim.

Measurement 231 (2024) 114661

Contents lists available at ScienceDirect

Measurement

journal homepage: www.elsevier.com/locate/measurement

Analysis of damage localization based on acoustic emission data from test of wind turbine blades

Adam Mielke [a,*], Hans-Henrik Benzon [b], Malcolm McGugan [b], Xiao Chen [b], Henrik Madsen [a], Kim Branner [b], Tobias K.S. Ritschel [a]

[a] Department of Applied Mathematics and Computer Science, Technical University of Denmark, Asmussens Allé, 303B, 2800 Kgs. Lyngby, Denmark
[b] Department of Wind and Energy Systems, Technical University of Denmark, Frederiksborgvej 399, 4000, Roskilde, Denmark

ARTICLE INFO

Keywords:
Acoustic emission
Damage localization
Structural health monitoring
Spatial analysis
Wind turbine blade

ABSTRACT

Acoustic emission (AE) is the transient elastic waves within a solid material caused by the rapid release of localized stress energy such as the formation of cracks when a material is subject to mechanical loading. This study investigates AE-signals generated from internal manufacturing flaws embedded in both a 14.3 m and a 31 m long wind turbine blade when they are under cyclic loading in a full-scale structural test. We are particularly interested in the spatial origin of these signals to localize damage within the structure. We perform spatial analysis on the frequency and energy of AE-signals and their positions in an industrial-scale blade. We find that, while tracing AE-signals back to the embedded manufacturing faults is straightforward, the acoustic wave properties are inconsistent throughout different test phases, which challenges the correlation between acoustic wave properties to the damage location. More reference test data should be collected to establish these correlations. This study provides insights into better utilizing AE-data for reliable structural health monitoring of wind turbine blades.

1. Introduction

Maintenance of wind turbines is a costly affair, in particular if these turbines are offshore where it is time consuming and expensive to get to. Difficult weather conditions also make maintenance more costly and can hinder access for long periods of time. This necessitates good structural health monitoring that allows remote detection of damage growth and other maintenance issues before a team is dispatched to make further investigations and possible repair [3]. Early detection of errors and the replacement of regular, and potentially unnecessary, inspections with predictive maintenance also greatly reduce costs [4,5]. This can be done both with passive and active systems [6], active being recording while applying an acoustic source, passive being recording without one.

We are particularly interested in exploratory analysis of acoustic emission (AE) data from existing projects where a 14.3 m blade and a 31 m blade, both with embedded artificial defects, were tested while being monitored by AE-sensors and as damage evolved from the artificial defects. AE-signal processing is a well-established method for recognizing damage growth and can be used as input for other methods to predict the lifetime of a number of materials and wind turbine blades in general [7–9]. These are often performed in controlled laboratory experiments to map out the signatures of damages to materials and structures. One of the great advantages of AE-signals is that the technology can be used on many different materials and is non-destructive.

Contribution of this paper

AE-signal processing has already been combined with spatial analysis, see for instance [10] and references therein, but the contribution of this paper is the combination of AE-data with spatial analysis in a full-scale test setting. Specifically, we analyze the frequency and energy of AE-signals and their positions compared to known faults. We do this for two different blades and compare the findings. The combination of frequency and energy is an established technique for finding damage signatures [11,12], but by including the estimated spatial location of the event, we gain more information than with frequency and energy alone. We also use the location to look at the parameters pairwise and distinguish between fault-related events and noise. Additionally, we indirectly gauge how close to the fault an AE-sensor has to be to pick up a characteristic signal. Importantly, we look at a full blade as opposed to coupons [11], as acoustic signals are probably different for industrial-scale blades and coupons.

Structure of the paper

* Corresponding author.
E-mail address: admi@dtu.dk (A. Mielke).

https://doi.org/10.1016/j.measurement.2024.114661
Received 30 January 2024; Received in revised form 28 March 2024; Accepted 3 April 2024
Available online 8 April 2024
0263-2241/© 2024 The Author(s). Published by Elsevier Ltd. This is an open access article under the CC BY license (http://creativecommons.org/licenses/by/4.0/).

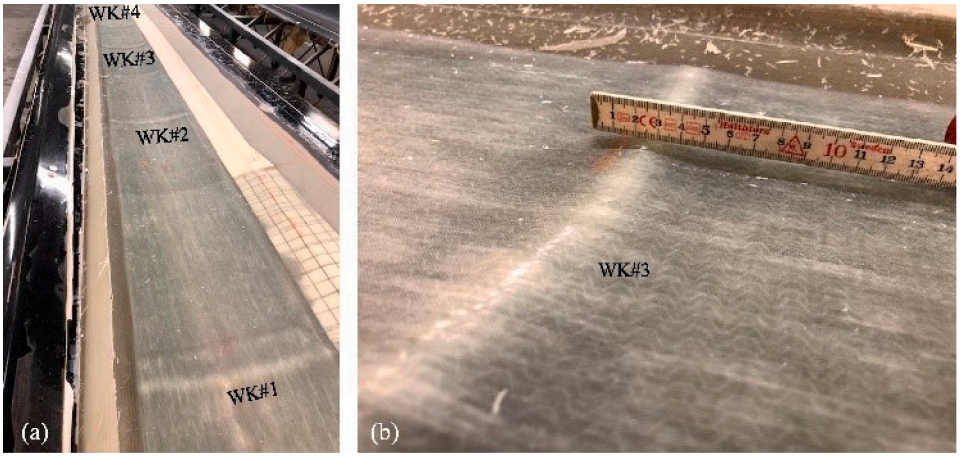

Fig. 1. Photo of the 14.3 m blade. Spar cap laminates are embedded with four resin inserts to create wrinkles during the manufacturing of the blade. (Both photos are also published in [1].) (a) The overview of four wrinkles with embedded resin inserts in the spar cap. (b) A close-up of Wrinkle 3.

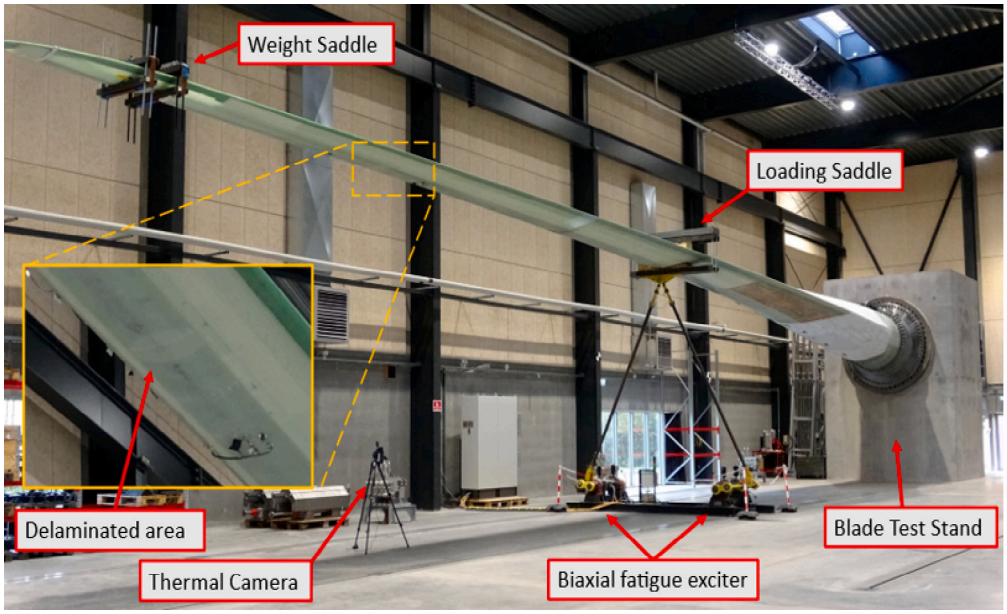

Fig. 2. Experimental setup of the 31 m long wind turbine blade under full-scale fatigue loading with AE sensors attached close to the delamination area. *Source:* Photo is also published in [2].

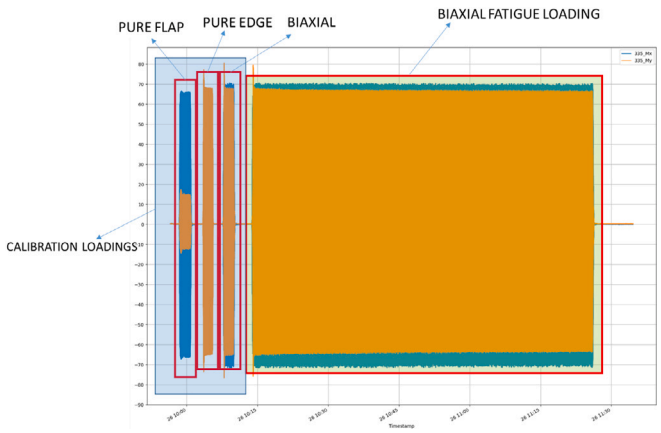

Fig. 3. Strain gauge output from one complete loading block, with the calibration and main fatigue loading sections indicated.

The paper is organized as follows. In Section 2, we describe the experimental setup and how the AE-data was gathered. In Sections 3 and 4, we go into details about how localization contributes to the analysis and how two different sensors may pick up different parameters from the same event. Then, in Section 5, deal with the data analysis, especially the connections between position, frequency, and energy over time, and compare blades of two different lengths. Finally, we discuss the results and make suggestions for future experiments in Section 7.

2. Basic experimental setup

2.1. Wrinkles in 14.3 m blade

Acoustic emission (AE) sensors are used to monitor the health of two wind turbine blades. The test loading of the 14.3 m blade was completed at the Large-Scale Test facility (LSF) at DTU Wind, RisøCampus between 24 March and 6 April 2021. It was manufactured by Olsen Wings [13] in Odder. Although based on a standard Olsen Wings product, the blade was a special manufacture that included four specifically designed embedded wrinkle defects along the spar cap, see Fig. 1. These defects would initiate and grow delamination damage when the blade was dynamically loaded.

A ground-based biaxial fatigue exciter mounted at $R = 5.2$ m on the blade was used to apply controlled dynamic forces and push the blade into oscillation. Forces can be applied in a blade flap- or edge-direction, or as a combination of the two. 9 AE-sensors were attached at various points: Two close to the root, and the rest distributed around the embedded wrinkles, see Fig. 4. (Note that the two sensors close to the root are not included on the figure as they are not relevant for our analysis.)

During the fatigue test, wrinkles caused delamination which further grew with the increase of fatigue cycle numbers. Acoustic emission signals were collected throughout the test campaign, divided into fifteen time blocks. Each block would begin with a set of calibration loadings. The first calibration set would consist of pure flap-load, this would be followed by a set of pure edge-load, and the final calibration set would be biaxial loading. After this calibration set was completed and checked for performance response, the main block of biaxial loading takes place. This biaxial fatigue loading would consist of approximately 10,000 cycles and take about 75 min to complete. This process (three calibration loadings followed by a 10,000 cycle main loading) would complete one loading block in the test series, see Fig. 3. The calibration data has not been used in our analysis.

The flap- and edgewise excitation frequencies were 2.3 Hz and 4.6 Hz respectively and the flapwise loading was at all times higher than the edgewise loading. It should be noted that there are two blades manufactured with identical artificial defects but they are tested differently. The one used in this study is tested as described above, but under different load scenarios from the one in [1]. The AE-system used for monitoring the test was a Sensor Highway III [14] from Physical Acoustics using PK15I sensors [15].

Analysis of the same experiment and data set, but without the localization can be found in [12]. We here look into the advantages and challenges of spatial analysis for this experiment. That is, if we pair up sensor hits based on whether they could have originated from the same location, we can attribute a more precise spatial component to the event which can both help identify and locate a fault.

2.2. Plydrop defect in 31 m blade

Acoustics emission data from a 31 m full-scale wind turbine blade with intentionally embedded severe plydrop defect at 25 m in the spar cap is also collected. The embedded defect triggered delamination growth in the spar cap when the blade is subject to constant cyclic loading for a total number of 320,000 cycles, see Fig. 2. Acoustic emission around the defect was detected by four sensors of the same type as above, attached to the outer surface of the blade. The AE sensors were placed at radius R = 23.95 m, 24.65 m, 25.35 m, and 26.05 m from the root of the blade in a linear array along the suction side spar cap. The following set up conditions and hit parameters were specified in the acquisition file. The set-up file for the sensors for the dynamic structure test specified a detection threshold of 45 dB (with a 12 dB gain). Timing parameters were Peak Definition Time 200 μs, Hit Definition Time 800 μs, Hit Lockout Time 1000 μs, and Max Duration of 500 ms. The detailed test setup can be found in [2].

3. The dataset and localization method

As digitizing the analog signal directly would require too high sample rate to be practical, a number of wave parameters are saved instead, see Fig. 5 for an illustration and explanation of these. The variables are of course highly correlated. For instance, the average frequency is found through the duration of a pulse and the number of threshold crossings. That is, frequency has perfect (though not linear) correlation with a combination of duration and the number of threshold crossings. When performing a principal component analysis, i.e., an eigenvalue decomposition of the covariance matrix to see which linear combinations of parameters contribute the most to the data, it is clear that the physical parameters can be reduced greatly. However, as we would like to keep the interpretation intact, we continue with the physical parameters.

A post-processing is made on the sensor hits to determine the likely event origin, see Fig. 6. This firstly involves pairing of the hits. The idea is that an event will emit a signal in two different directions, and by pairing two hits we can find the original location. Very few (<0.1%) of the sensor hits have more than one possible partner in adjacent sensors within the travel time of a sound wave. There is therefore very little ambiguity in the pairing. However, a lot of hits are discarded (~90%) because no partner is found. As the scale of time-differences between two pairs is significantly larger than the travel time between sensors, it is unlikely that the loss comes from different hits overlapping. It is also clear that the loss happens more frequently in the later blocks, which suggests that fewer events reach two sensors, see Fig. 7.

For completeness, we briefly go through the mathematics of this localization. Let us assume we have two hits at times and locations (t_1, x_1) and (t_2, x_2) that we know correspond to the same event at (t_0, x_0). Let us for simplicity assume that $x_2 \geq x_0 \geq x_1$, that is, that the event happens between the two AE-sensors. We may then write

$$\begin{aligned}(t_2 - t_0)v &= x_2 - x_0 \\ (t_1 - t_0)v &= x_0 - x_1\end{aligned} \tag{1}$$

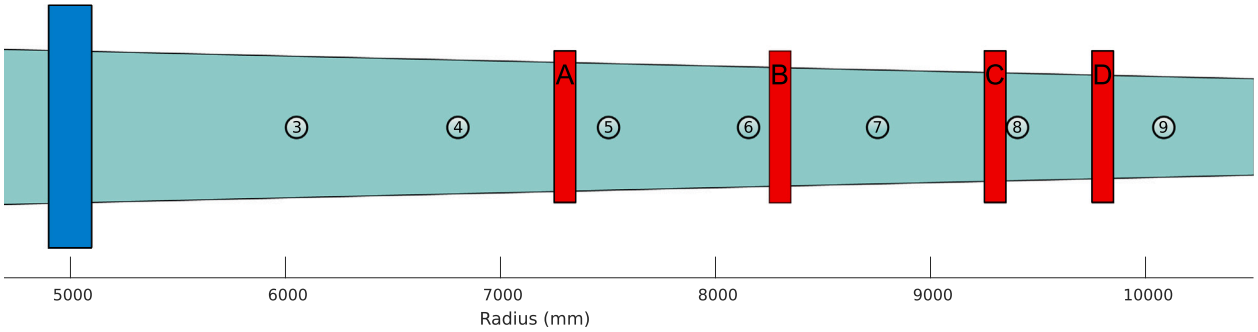

Fig. 4. Schematic of the 14.3 m blade with the AE-sensors marked. The large blue block indicates the attachment of the blade exciter, and the smaller red blocks indicate the faults. CH1 and CH2 are outside the plot on the left.

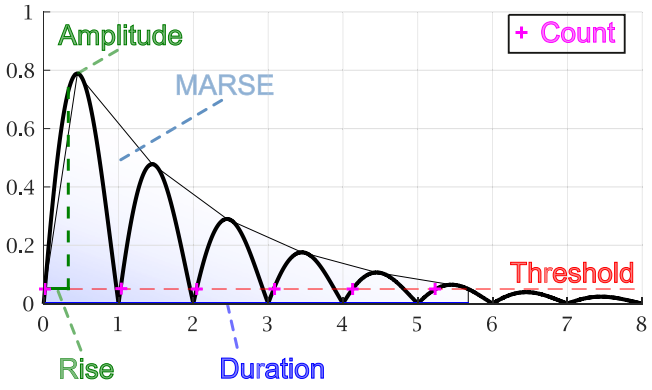

Fig. 5. Illustration of the variables that are recorded for each event. The amplitude is the height of the event, the count is the number of threshold crossing, the rise is the time from first crossing to highest point, and the duration is the time from first to last threshold crossing. The energy is calculated from an approximation of the wave envelope (MARSE).

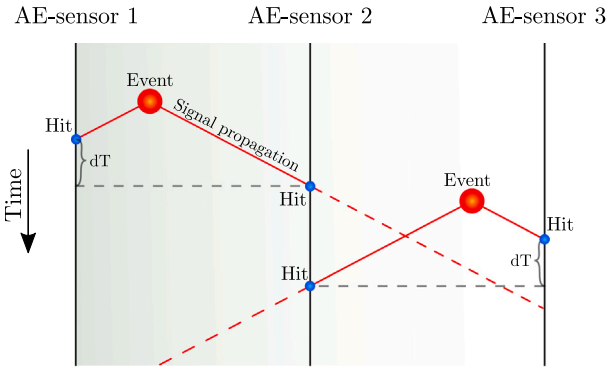

Fig. 6. Illustration of how the acoustic events are registered by the AE-sensors and subsequently how the event position is estimated. By pairing the hits based on time difference, dT, and assuming a value of the speed of sound, the measured hits can be traced back to find the original event. The dashed lines indicate that pulses are heavily dampened in the medium and therefore hardly ever are picked up by more than the two adjacent sensors.

where using $v \approx 2$ km/s for the 14.3 m blade and $v \approx 2.5$ km/s for the 31 m blade as the average speed of sound in the medium gives a good approximation for initial sensor tests where the blade is struck to test the localization. This leads us to

$$x_0 = \frac{x_2 + x_1}{2} - v\frac{t_2 - t_1}{2}$$
$$t_0 = \frac{t_2 + t_1}{2} - \frac{x_2 - x_1}{2v} \quad (2)$$

So the event time and place are based on the deviation from the corresponding means. (Note that the sign of $t_2 - t_1$ determines whether x_0 is larger or smaller than the midpoint.) See Fig. 7 for a plot of these locations and times, and Fig. 13 in Appendix for comparison between the time, location, and either MARSE energy or frequency. Most of the faults are faintly visible in the data. However, there are clear discontinuities across channels, and some intervals have very few points. This suggests that part of the signal is stopped before reaching another sensor. Note that a uniform and constant speed of sound in the medium is an approximation, and some discrepancy between the actual source and the localized source may occur.

4. AE-event properties

The damping we indicate in Fig. 6 is directly observable in the data by plotting the differences in measurements for the first and second sensors in the pair as a function of the time difference between the hits. The time difference is of course proportional to the difference in distance traveled, see Fig. 8 for this plot. Specifically, the amplitude difference increases as a function of difference in distance, which indicates that the waves are quite dampened. This is also why we do not see the events on more than two sensors. Ideally, we would like to have several observations of the same event, but with the current setup this has not been possible.

While it is possible that the damping affects the localization accuracy, the fact that several of the faults are observable as areas of increased point density in Fig. 7 suggests that this is a minor effect.

Notice also in the same figure that the MARSE energy has the same behavior as amplitude, which is natural as they are positively correlated. The differences for the time parameters rise and duration also increase with the time differences between hits, so the wave packets are both shorter and weaker. However, the frequency is symmetric, which suggests that this information is preserved on average.

5. Wave parameters versus location

We would like to have some observable that can work as a proxy for the fault sizes and give us the approximate location of the fault. It seems that frequency is the best-suited for this, see Figs. 9 and 10. Though somewhat noisy, it is clear that the faults are visible as peaks of higher frequencies, apart from simply being an area of more events.

For the energy, there is a bulk of small values along with a group of outliers that moves further away over time for the 14.3 m blade. However, the outliers are also present in the interval between Channels

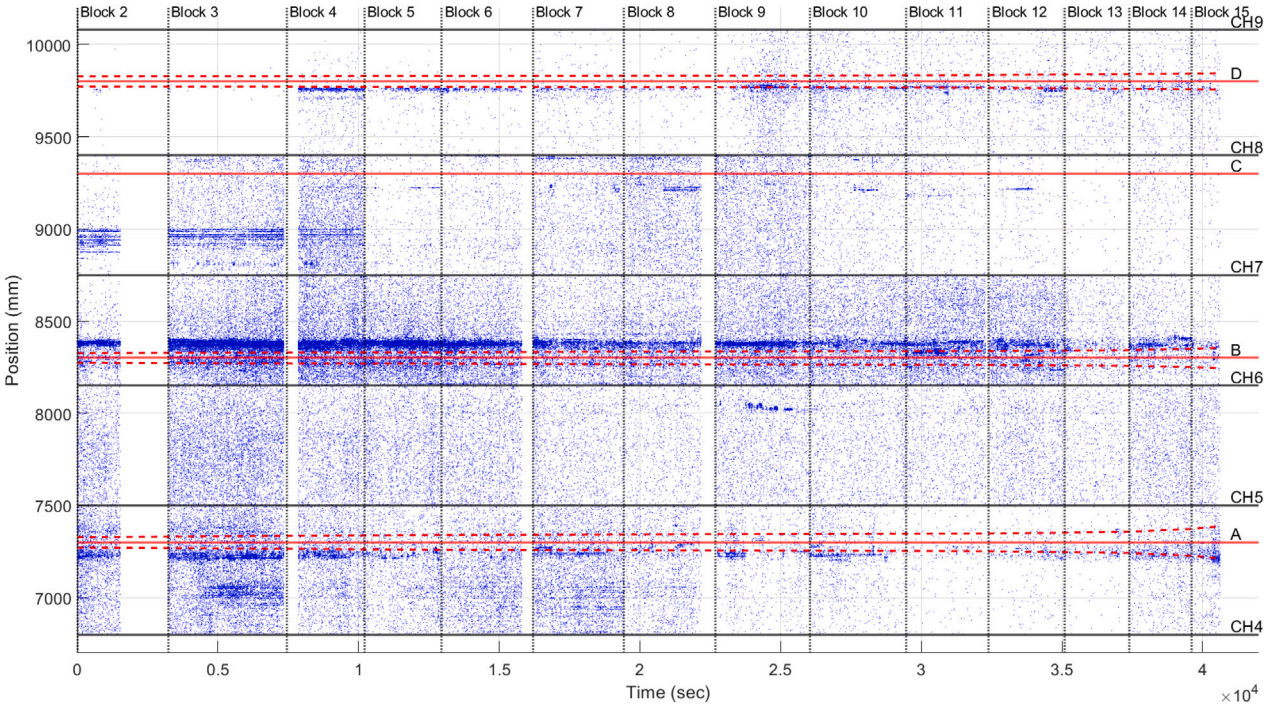

Fig. 7. The time and location (t, x) of each event in the paired data for the 14.3 m blade. That is, each acoustic event that the pairing and localization algorithms find is plotted to illustrate the development over time. The speed of sound is set to $v = 2$ km/s. The dotted vertical lines indicate blocks. We see a clear thinning of points in the later blocks, possibly because the signal from an event only reaches one sensor and is therefore discarded. The known faults are also plotted, along with the width for those of which that have known widths. Most of the faults are faintly visible in the data apart from Wrinkle C, which is hidden beneath a DIC measurement layer. We also see that wrinkle B was most critical with most damage growth. The cluster below Wrinkle C is likely some outside source of consistent noise, such as wires or a loose piece of material inside the blade.

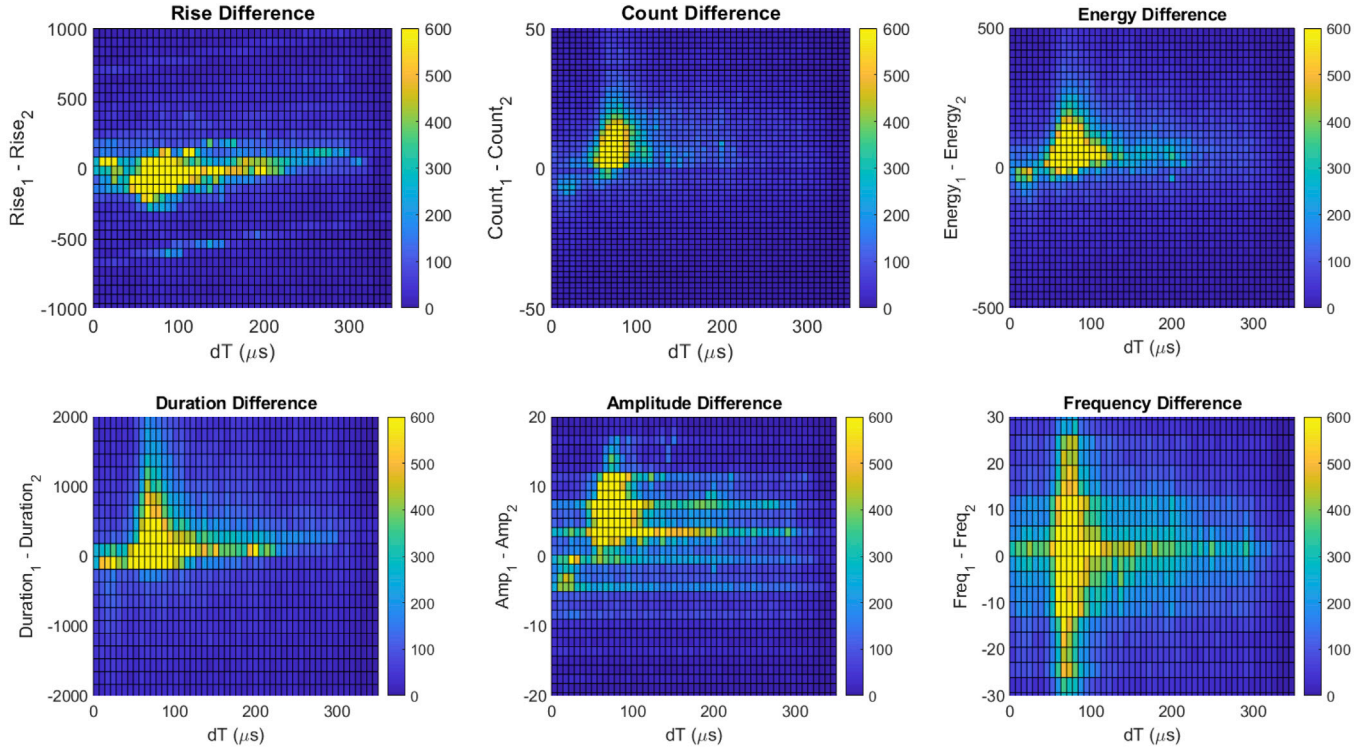

Fig. 8. Comparison of difference of variables for first and last triggered sensor, 1 denoting the first sensor and 2 the second, i.e. $var_1 - var_2$. Note that all variables but the frequency are asymmetric, indicating that they are dampened over distance. They are all plotted as a function of the time difference dT, which is proportional to the difference in distance traveled.

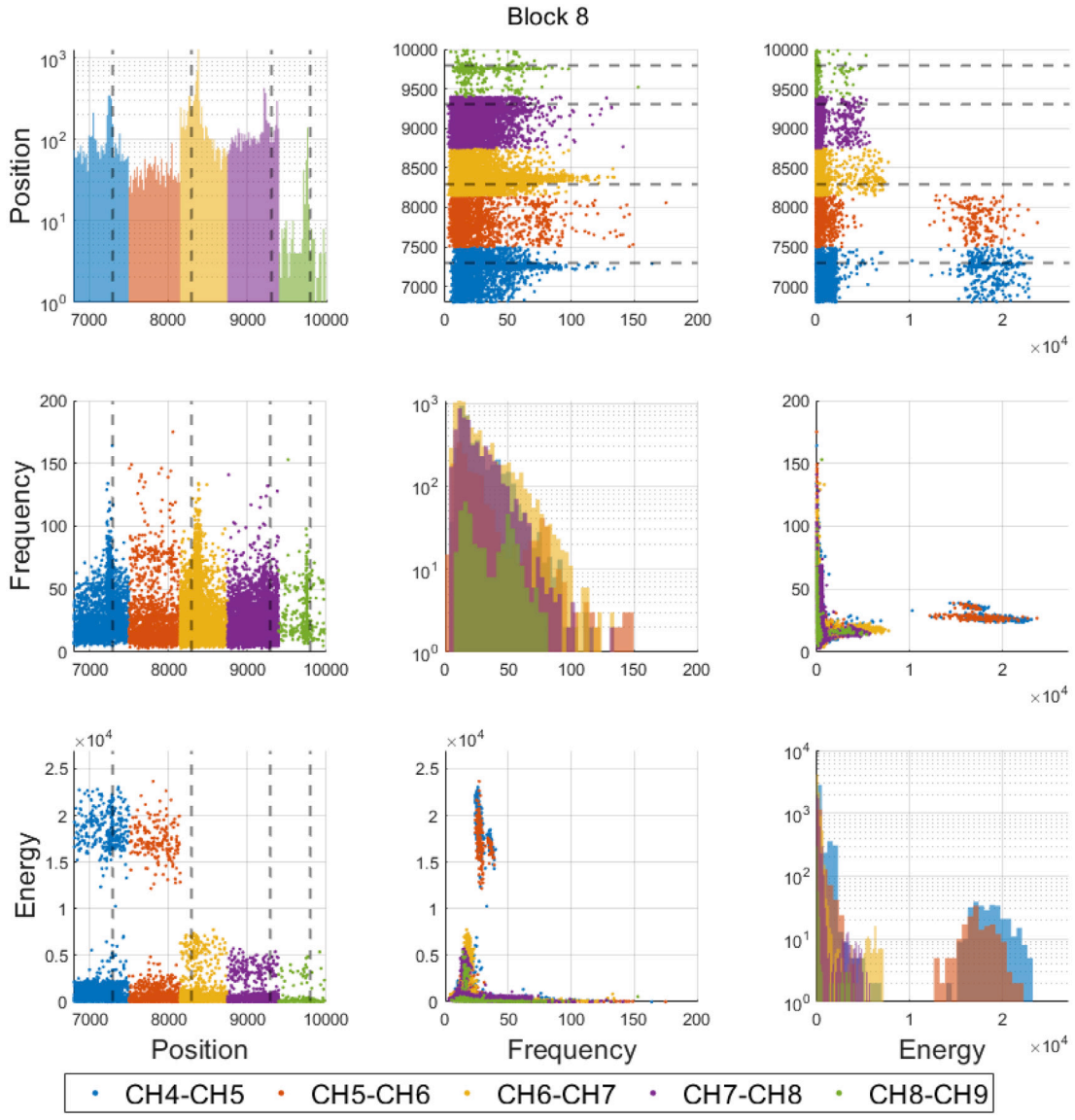

Fig. 9. Location versus frequency and energy for block 8 of the 14.3 m blade as an example. (The other blocks are qualitatively similar, though the energy outliers move further away over time.) Where rows and columns coincide, we have plotted histograms of the given variable, and where they differ, we have plotted scatter plots of the two variables. The faults have been marked on the position plots as dashed lines, and the data points are colored by interval between channels. For the scatter plots, both transpositions are included, such that the comparison with the histograms (note that they are on log-scale) can easily be made for all variables.

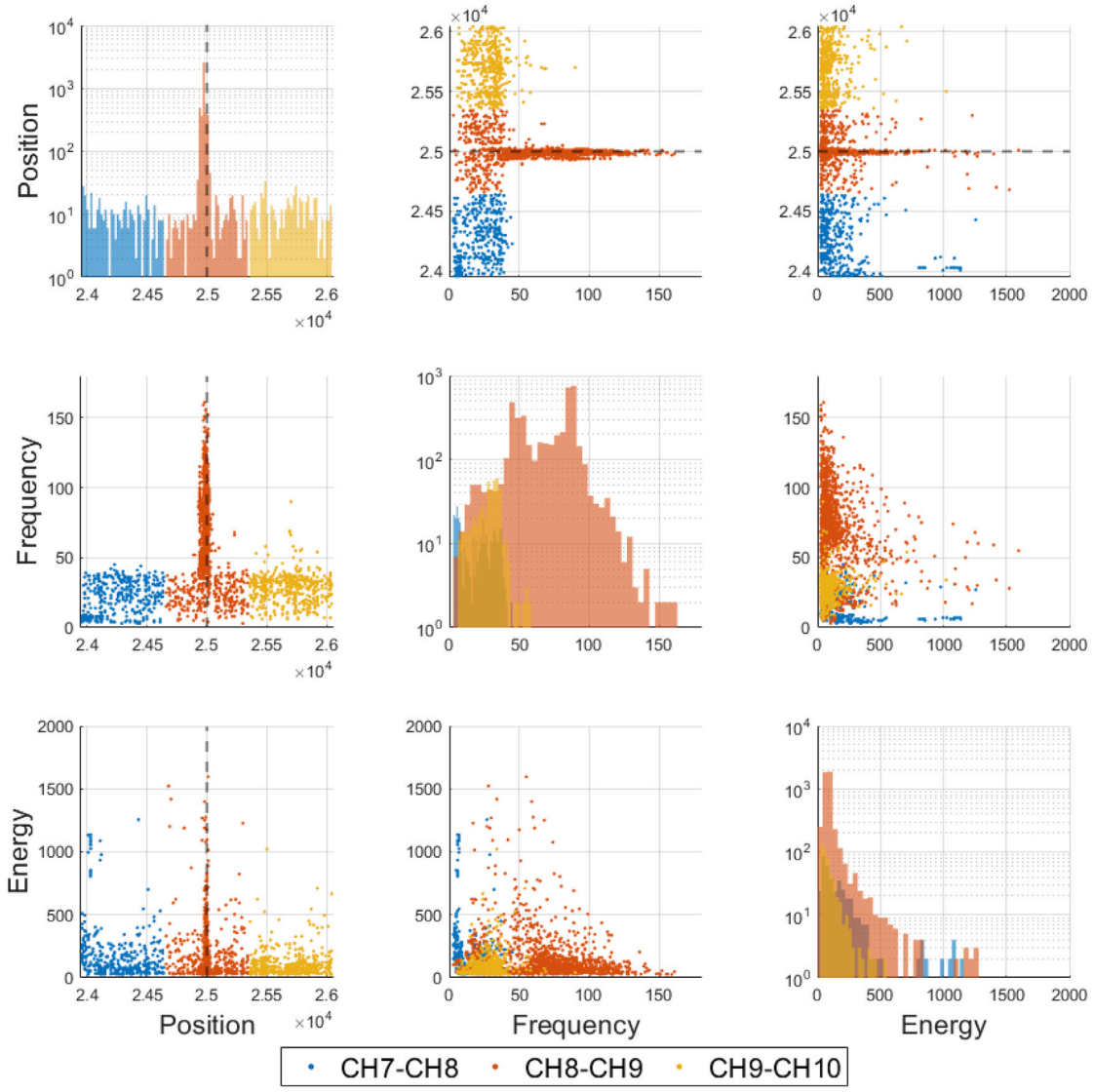

Fig. 10. Location versus frequency and energy for the 31 m blade. The single fault has been illustrated on the position plots with a dashed line, and the data points are colored by interval between channels. Where rows and columns coincide, we have plotted histograms of the given variable, and where they differ, we have plotted scatter plots of the two variables. For the scatter plots, both transpositions are included, such that the comparison with the histograms (note that they are on log-scale) can easily be made for both position and frequency.

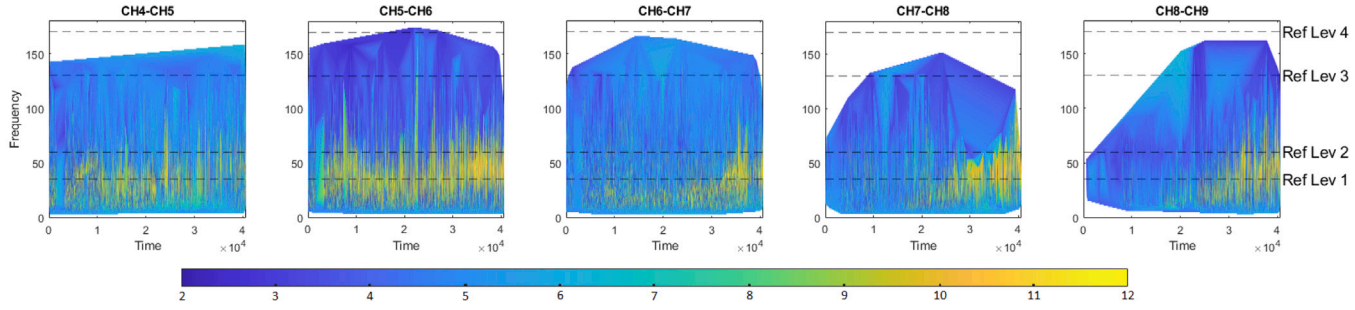

Fig. 11. The energy in each part of the frequency spectrum as a function of time for each interval for the 14.3 m blade. The color (blue to yellow) indicates the MARSE energy on log scale. The black horizontal lines indicate the average frequencies found for different types of damages in [16], where the reference levels are micro-cracking (Ref Lev 1), delamination (Ref Lev 2), matrix cracking (Ref Lev 3), and fibre matrix debonding (Ref Lev 4). These are for different materials and setups, so we do not expect a one-to-one correspondence, but they are included to guide the eye.

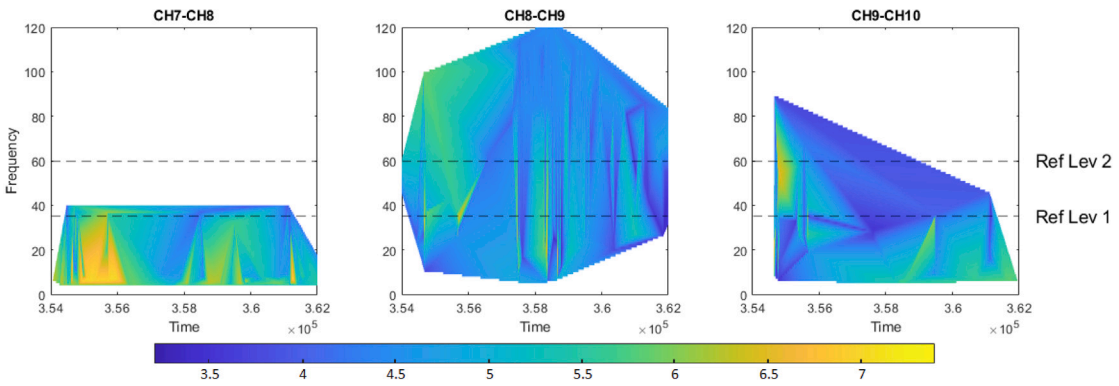

Fig. 12. The energy in each part of the frequency spectrum as a function of time for each interval for the 31 m blade. The color (blue to yellow) indicates the energy on log scale. The black horizontal lines indicate the average frequencies found for different types of damages in [16], where the reference levels are micro-cracking (Ref Lev 1), delamination (Ref Lev 2), matrix cracking (Ref Lev 3), and fibre matrix debonding (Ref Lev 4). These are for different materials and setups, so we do not expect a one-to-one correspondence, but they are included to guide the eye. We see that there is no pattern around 50–60 kHz as in Fig. 11. It should also be noted that the color scale for the 31 m blade has a lower maximum than the 14.3 m blade.

5 and 6 (the second from the left), which does not have a wrinkle. The actual interval that stands out regarding energy is the middle one (the one between Channels 6 and 7), but Wrinkle B is present there.

The noise around the frequency indication does not seem to be present when looking at the larger blade. The 31 m blade was tested for a shorter period of time (only one block), but the separation is much clearer, compare Figs. 9 and 10. The reason for this is most likely that the eigenmodes of the longer blade have longer wavelengths, which make the fault stand out more in the higher frequency domain. Note also how the less clear connection between frequency and MARSE energy, visible in Fig. 12, can be seen here in Fig. 10 as well.

However, looking at the data in terms of frequency versus energy over time in different channel intervals, the placement of indicators is still more ambiguous than we would like. Although the energy of different frequency bands is a good indicator for which sensors have a fault next to them [12], the actual origin of the signal is much less clear, see Fig. 11 for the 14.3 m blade. It shows the frequency as a function of time with the MARSE energy as the color and different reference levels from coupons in [16]. There are also damage patterns available in [17], but these mostly lie outside the interval of frequencies we observe. We see that, although a damage-like pattern occurs, a lot of the signal seems to come from the interval CH5-CH6, which does not have an embedded fault. That is, if we associate the energy and frequency with a localized event rather than a sensor-hit, we find that the interval without any faults still has a larger amount of energy in the delamination and micro-cracking frequency range. Also, note that this signal is absent for the 31 m blade, see Fig. 12. This may be because the damage type is different. The overall scale of the energy is also smaller for the 31 m blade than the 14.3 m blade. It is possible that this is caused by a micro-cracking signal appearing throughout the entire blade.

The band of events around 50–60 kHz with higher energy that can be seen in Fig. 11 is also faintly visible in the frequency/position plots in Fig. 9.

6. Discussion

Looking at Fig. 7, it is clear that we are able to trace the positions of the events to the embedded faults throughout the test. The only exception is Wrinkle C, which is hidden beneath a digital image correlations measurement layer.

However, when relating the wave parameters to the position, things become less clear in the energy regime, but more clear in the frequency regime, as can be seen in Figs. 9–12. High frequency seems related to the development of faults and correlates with the positions of the embedded defects, whereas high energy is related to a particular frequency band.

Although the interval between CH5 and CH6 contains no faults, it exhibits a lot of the properties associated with damage, such as high-energy events at the 50 kHz band, to an even greater extend than the other intervals. It is possible that the cracking is more pronounced in smooth areas (i.e. intervals without defects) or that the signal from the wrinkles is reflected in different places.

7. Conclusion and outlook

We have analyzed acoustic emission data from two different wind turbine blades with particular emphasis on the localization of the events. We find that the distribution of positions is consistent with the embedded faults and that the damping of the signal over distance is directly observable. We find that high frequency is directly relatable to the fault location, but we have difficulties relating the other acoustic wave properties to the expected locations.

As the main difficulty with the current dataset is ambiguity, the suggestion for future improvement of the experimental setup is having more references. The simplest reference would be a spatial calibration at the beginning of each block. By striking the blade at known positions to excite waves in the kHz-regime, it could be confirmed whether or not the pulses can propagate to sensors on both sides, thus keeping track of any loss through damping. Note that AE-sensors are easy to trigger, so simply knocking on the blade with a knuckle or a hammer is enough. We suggest equidistant strikes along the blade with at least a couple of strikes in each sensor interval. If a certain section is found to dampen the signal, it also allows extra sensors to be set up on either side of the area and minimize the loss from it. This is of course impractical to do on a wind turbine in service, but it would help the physical understanding.

Additionally, but more costly, having a reference blade with no manufactured faults for comparison would improve understanding of the baseline. Testing more type of blades to characterize fault types based on AE-signal would also be a natural next step. This would also allow test of environmental factors such as temperature and humidity.

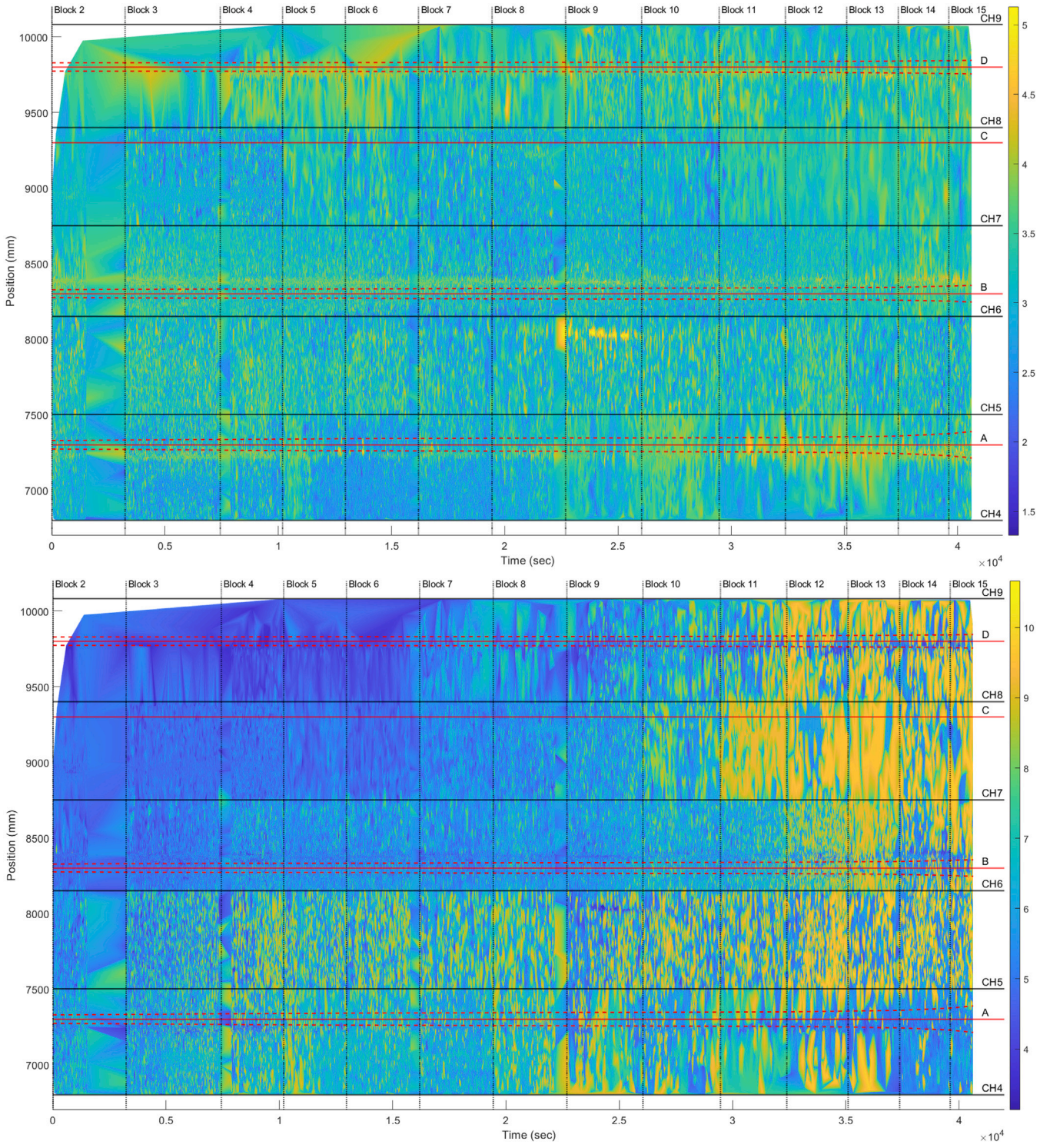

Fig. 13. Plot for the 14.3 m blade of time versus position with frequency (top) and MARSE energy (bottom) on the color axis, both on log-scale. There seems to be a signal of higher frequency along the faults, especially at Wrinkle B, whereas the MARSE energy is much more spread out. Note that Fig. 9 looks at Block 8 of this plot.

CRediT authorship contribution statement

Adam Mielke: Writing – review & editing, Writing – original draft, Visualization, Software, Formal analysis, Data curation, Conceptualization. **Hans-Henrik Benzon:** Methodology, Conceptualization, Software, Writing – review & editing. **Malcolm McGugan:** Writing – review & editing, Writing – original draft, Visualization, Supervision, Software, Methodology, Investigation, Data curation, Conceptualization. **Xiao Chen:** Writing – review & editing, Writing – original draft, Supervision, Project administration, Funding acquisition, Conceptualization. **Henrik Madsen:** Writing – review & editing, Supervision, Project administration. **Kim Branner:** Conceptualization, Funding acquisition, Project administration, Supervision, Writing – review & editing. **Tobias K.S. Ritschel:** Conceptualization, Formal analysis, Project administration, Supervision, Writing – review & editing.

Declaration of competing interest

The authors declare that they have no known competing financial interests or personal relationships that could have appeared to influence the work reported in this paper.

Data availability

Data will be made available on request.

Acknowledgments

This study was funded by the RELIABLADE project (Improving Blade Reliability through Application of Digital Twins over Entire Life Cycle, 64018-0068) through the Energy Technology Development and Demonstration Program (EUDP) of Denmark.

Appendix. Energy and frequency as functions of time and position

For completeness, and to give context to Fig. 9, we also show the dependence of the MARSE energy and frequency for the 14.3 m blade as a function of position and time for the whole run, see Fig. 13. There the wrinkles are visible as bands of slightly increased frequency, whereas the MARSE energy is spread out over the entire blade.

References

[1] X. Chen, S. Semenov, M. McGugan, S.H. Madsen, S.C. Yeniceli, P. Berring, K. Branner, Composites A 140 (2021).
[2] S.S. Samareh-Mousavi, X. Chen, M. McGugan, S. Semenov, P. Berring, K. Branner, N. Ludwig, Struct. Health Monit. (2024) in press.
[3] M. McGugan, G.F. Pereira, B.F. Sørensen, H.L. Toftegaard, K. Branner, Phil. Trans. R. Soc. A 373 (2015).
[4] N. Luo, Y. Vidal, L. Acho (Eds.), Wind Turbine Control and Monitoring, Springer, 2014.
[5] W. Wang, Y. Xue, C. He, Y. Zhao, Energies 15 (15) (2022).
[6] M.A. Fremmelev, P. Ladpli, E. Orlowitz, N. Dervilis, M. McGugan, K. Branner, Struct. Health Monit. 22 (6) (2023) 4171–4193.
[7] M. Saeedifar, D. Zarouchas, Composites B 195 (2020) 108039, http://dx.doi.org/10.1016/j.compositesb.2020.108039.
[8] M.A. Fremmelev, P. Ladpli, E. Orlowitz, L.O. Bernhammer, M. McGugan, K. Branner, Data-Cent. Eng. 3 (2022) e22, http://dx.doi.org/10.1017/dce.2022.20.
[9] W. Zhou, Z. Pan, J. Wang, S. Qiao, L. Ma, J. Liu, X. Ren, Y. Liang, J. Mater. Sci. 58 (2023) 483–607.
[10] L. Dong, Q. Tao, Q. Hu, S. Deng, Y. Chen, Q. Luo, X. Zhang, Int. J. Mining Sci. Technol. 32 (3) (2022) 487–497.
[11] R.A.A. Lima, R. Tao, A. Bernasconi, M. Carboni, S.T. de Freitas, Composites B (2023).
[12] H.-H. Benzon, A. Mielke, T.K.S. Ritschel, M. McGugan, K. Branner, X. Chen, in preparation.
[13] (Olsen Wings). https://olsenwings.dk/.
[14] (Sensor Highway III). https://www.physicalacoustics.com/by-product/sensor-highway-iii.
[15] (AE-Sensor). https://www.physicalacoustics.com/content/literature/sensors/Model_PK15I.pdf.
[16] A.A. Lima, R. Taob, A. Bernasconia, M. Carbonia, S.T. de Freitas, JCOMB-D-23-04111.
[17] P.J. de Groot, P.A.M. Wijnen, R.B.F. Janssen, Compos. Sci. Technol. (55) (1996).